





FEASIBILITY STUDY FOR A FUEL CELL-POWERED UNMANNED AERIAL VEHICLE WITH A 75 KG PAYLOAD

José M. Desantes , Ricardo Novella , Luis M. García-Cuevas *, Marcos Lopez-Juarez 
CMT-Motores Térmicos. Universitat Politècnica de València. Camino de Vera s/n, 46022 Valencia, Spain.

Abstract

Among the possible electric powerplants currently driving low-payload UAVs (up to around 10 kg of payload), batteries offer certain clear benefits, but for medium-payload operation such as aerotaxis and heavy-cargo transportation UAVs, battery capacity requirements restrict their usage due to high weight and volume. In light of this situation, fuel cell (FC) systems (FCS) offer clear benefits over batteries for the medium-payload UAV segment (> 50 kg). Nevertheless, studies regarding the application of FCS powerplants to this UAV segment are limited and the in-flight performance has not been clearly analysed. In order to address this knowledge gap, a feasibility analysis of these particular applications powered by FCS is performed in this study. A validated FC stack model (40 kW of maximum power) was integrated into a balance of plant to conform an FCS. As a novelty, the management of the FCS was optimized to maximize the FCS efficiency at different altitudes up to 12500 ft, so that the operation always implies the lowest H₂ consumption regardless of the altitude. In parallel, an UAV numerical model was developed based on the ATLANTE vehicle and characterized by calculating the aerodynamic coefficients through CFD simulations. Then, both models were integrated into a 0D-1D modelling platform together with an energy management strategy optimizer algorithm and a suitable propeller model. With the preliminary results obtained from the FCS and UAV models, it was possible to ascertain the range and endurance of the vehicle. As a result, it was concluded that the combination of both technologies could offer a range over 600 km and an endurance over 5 h. Finally, with the integrated UAV-FCS model, a flight profile describing a medium altitude, medium endurance mission was designed and used to analyse the viability of FC-powered UAV. The results showed how UAVs powered by FCS are viable for the considered aircraft segment, providing competitive values of specific range and endurance.

Keywords: Unmanned Aerial Vehicle, fuel cell, hydrogen, optimization

Type of the work: research article

List of symbols

α	Charge transfer coefficient
C	Transport loss coefficient
C_D	Drag coefficient
$C_{D,0}$	Parasitic drag coefficient
C_L	Lift coefficient
C_p	Power coefficient
C_t	Thrust coefficient

$\Delta\bar{g}_f$	Released Gibbs free energy	J mol ⁻¹
D	Propeller diameter	m
dt	Time step	s
η_{DC-DC}	Efficiency of the direct-current voltage conversion stage	
η_{FCS}	Efficiency of the fuel cell system	
η_m	Efficiency of the electric motor	
η_p	Propeller propulsive efficiency	
F	Faraday constant	C mol ⁻¹
I	Fuel cell stack current	A
i	Current density	A m ⁻²
i_l	Limiting current density	A m ⁻²
i_0	Exchange current density	A m ⁻²
$i_{0, ref}$	Reference exchange current density	A m ⁻²
J	Advance ratio	
k_1	First coefficient of the drag due to lift coefficient	
k_2	Second coefficient of the drag due to lift coefficient	
\dot{m}_{H_2}	Hydrogen mass flow	kg s ⁻¹
MW_{H_2}	Molecular mass of H ₂	kg mol ⁻¹
n	Rotational speed	Hz
n_{cell}	Stack number of cells	
P_{FCS}	Power output of the fuel cell system	W
P_{mb}	Propeller brake power	W
P_{me}	Electric power output of the direct-current voltage converter	W
P_t	Thrust power	W
ρ	Air density	kg m ⁻³
R_{gas}	Gas constant	J mol ⁻¹ K ⁻¹
R_{ohm}	Ohmic resistance	Ω
T	Temperature, propeller thrust	K, N
t	Time	s
u	Air speed	m s ⁻¹
ω	Rotational speed	rad s ⁻¹
V_{act}	Activation losses	V
V_{FC}	Voltage of the fuel-cell stack	V
V_{mt}	Mass transport (concentration) losses	V
V_{OC}	Open circuit voltage	V
V_{ohm}	Ohmic losses	V
W	Aircraft weight	N
y^*	Non-dimensional distance to the wall	
AC	Alternate current	
BoP	Balance of plant	
DC	Direct current	
FC	Fuel cell	
FCS	Fuel cell system	
MTOM	Maximum take-off mass	
OEM	Operating empty mass	
PID	Proportional-integral-derivative controller	
UAV	Unmanned air vehicle	

1. INTRODUCTION

The ambitious goals of the Paris agreement are leading to important changes in most sectors of human activity. From food production and goods manufacturing to shipping and urban transport, electrification and the use of carbon-neutral fuels are some of the keys to achieve these goals. Aligned with this, the European Green Deal [1] has been presented as a cornerstone policy of the European Union to achieve our common international commitments, and the aviation sector will need to adapt and reach climate neutrality by 2050. Continuing on from the works produced during the Clean Sky and Clean Sky 2 Joint Undertakings, the European Partnership for Clean Aviation [2] will be built to radically reduce the aviation sector's environmental impact. For this, Europe is clearly betting on green hydrogen, which will be produced by water electrolysis using renewable electrical energy. Several approaches could then be taken and are being actively researched: use it in the production of synthetic sustainable aviation fuel as in [3], burn it in reciprocating internal combustion engines (both in spark ignition such as in [4] or in compression ignition such as in [5] or jet engines as in [6] or use it in fuel cells to produce electrical power. For very small aircraft with very low endurance missions, battery-electric propulsion has proven to be a viable and cost-effective solution.

The way to decarbonise the aviation sector is somewhat clear for very small aircraft such as small unmanned air vehicles (UAV) and big airliners, but it is not as obvious for intermediate mass vehicles. Personal air vehicles or big UAVs for urban transport applications are examples of such vehicles, in which the energy and power density of the batteries available today are prohibitively small for most applications except short trips. Although jet engines or internal combustion engines might be used, they incur high levels of noise pollution and it is still non-obvious how to make them burn without producing CO₂ or NO_x while keeping very high power densities. This segment also benefits from (and sometimes requires) distributed electric propulsion approaches, using multiple propellers that are used for vertical take-off and landing and for forward flight, which introduces extra elements for mechanical power to electrical power conversion. Fuel cell systems (FCS) are an attractive alternative: they present greater efficiencies than combustion engines, directly produce electrical power, have fewer moving parts, work silently and, depending on the technology, run much colder. Although they achieve lower power densities than combustion engines and they degrade fast when producing high current and power outputs, their advantages over other alternatives may lead them to become a good technological solution for medium-sized, low-to-moderate speed aircraft. Indeed, FCS are being investigated by the industry for other segments, as presented by Baroujati et al. [7]. To the best of our knowledge, however, very little has been published in the literature about the use of fuel cells in this segment, so it is difficult to ascertain whether they are a viable power source.

1.1. Objectives and contributions

In light of the scenario described in section 1, this study aims to understand the feasibility of using FCS as the powerplant of UAVs. To accomplish this main objective, this study is intended to make the following contributions to the research on the use of FCS in UAV:

- Generate a fully integrated FCS-UAV numerical model including the UAV aerodynamics, FCS, battery, H₂ tank, electric motor and propeller components to simulate steady-state conditions and missions.
- Generate the performance maps describing the capabilities of the FCS-UAV binomial in terms of specific range (flight distance per unit mass of fuel), specific endurance (flight time per unit mass of fuel), systems efficiency and flight conditions.
- Simulate a medium-range medium-endurance mission with a varying altitude profile to understand the performance of the FCS-UAV vehicle in realistic flight conditions.

2. METHOD

This section describes the methodology followed for the fulfilment of the objectives described in section 1.1. It is composed of a first section in which the models are developed and integrated (sections 2.1, 2.2, and 2.3) and a second section in which the mission is defined and simulated (section 2.4).

2.1. UAV aerodynamic model

The aerodynamic performance of the UAV is computed using a drag polar curve of the form presented in Eq. (1):

$$C_D = C_{D,0} + k_1 C_L + k_2 C_L^2 \quad (1)$$

where C_D is the drag coefficient, $C_{D,0}$ is the parasitic drag coefficient, C_L is the lift coefficient and k_1 and k_2 are fitting parameters. The fitting constants are calibrated against computational fluid dynamics (CFD) simulations. The results of the CFD simulations were almost independent of the Reynolds number variations that were expected for the missions studied in this work, so a single set of fitting parameters were obtained. The CFD simulations were carried out using a grid of 7.7 million cells and a Reynolds-averaged Navier-Stokes approach for the turbulence effects, which were modelled by means of the two-equations $k - \omega$ SST turbulence model by Menter. A prismatic layer of cells growing in geometric progression was used near the aircraft surface to ensure a non-dimensional wall distance to the centroid of the first cells y^+ equal or lower than 1, so the viscous region of the boundary layer could be solved. The solution was computed iteratively until convergence of C_L and C_D between -2° and 8° of angle of attack.

2.2. Propulsion system model

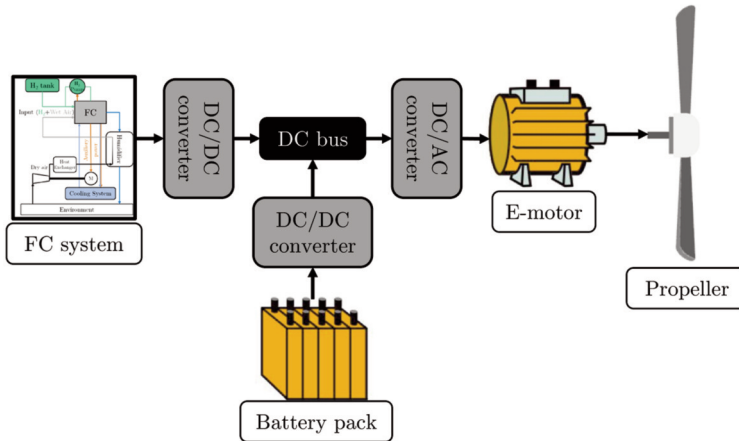


Figure 1. Powerplant components outline, indirect-type FCV architecture.

The powerplant of the target UAV is composed by the usual components found in fuel cell vehicles (FCV) together with a suitable propeller sized for the desired application. As such, the propulsion system comprises the FCS, in charge of producing most of the power during the UAV operation, the battery, used to provide additional power when required for in-flight performance, take-off and landing operation, the electric motor, which converts the electrical power into mechanical power for the propeller, and

the propeller, in charge of converting mechanical power into thrust power. Note that for the mission in this study the battery was included to provide a complete powerplant model but was not used since take-off and landing were not modelled, and during all the mission the power produced by the FCS was enough to make the UAV flight in the desired conditions. A sketch for these systems interconnection can be found in Figure 1. These models are connected to the UAV aerodynamic model in such a way that the powerplant components' operation is adjusted to the optimum operating condition for the desired flight condition.

2.2.1. Fuel cell system model

The FCS model used was developed on previous work for automotive applications [8, 9] and scaled down for the activities performed in this study. It consists of an FC stack together with all the components required for the management of the flows going to and coming from the stack, i.e., the balance of plant (BoP). To model these components, the software GT Suite v2020 was used. This modelling platform is widely used in the automotive industry for the 0D-1D modelling of thermofluid-dynamics and provides an accurate description of the flow behaviour by applying the energy, mass, momentum and species conservation equations together with widely-applied correlations.

The voltage of the FC stack for a given current density provides information about the power produced in the stack for a given flow of protons (H^+) through the membrane. The evolution of the voltage with current density is described by the polarization curve, described as in Eq. 2:

$$V_{FC} = V_{OC} - V_{act} - V_{ohm} - V_{conc} \quad (2)$$

$$V_{OC} = \frac{-\Delta\bar{g}_f}{2F} \quad (3)$$

$$V_{act} = \begin{cases} \frac{R_{gas}T}{2F} \left(\frac{i}{i_0} \right) \\ \frac{R_{gas}T}{2\alpha F} \log \left(\frac{i}{i_0} \right) \end{cases} \quad (4)$$

$$V_{ohm} = R_{ohm} I \quad (5)$$

$$V_{mt} = -C \log \left(1 - \frac{i}{i_0} \right) \quad (6)$$

where V_{OC} is the open voltage circuit and V_{act} , V_{ohm} and V_{mt} are the activation, ohmic and mass transport (concentration) losses. Additional models were used to describe the change in the ohmic resistance and the exchange current density to the stack operating conditions. Ohmic resistance (R_{ohm}) was modelled following the correlation proposed by Terada et al. [10] that described the dependence of the membrane ionic conductivity on the membrane water content, temperature and properties. The exchange current density (i_0) was modeled as a function of the FC temperature, the oxygen partial pressure, the electrochemical activation energy, the electrode roughness and the reference exchange current density $i_{0, ref}$ [11].

The polarization curve was validated with experimental data [12,13] by calibrating the mass transport loss coefficient (C), the charge transfer coefficient (α), the reference exchange current density ($i_{0, ref}$),

the limiting current density (i_l) and the open circuit voltage losses included in V_{OC} . The value of these parameters was calibrated by using the genetic algorithms design optimizer of GT Suite v2020 at different conditions of cathode inlet pressure and stack temperature so that the stack can be operated at a wide range of operating conditions achieving an overall error of 2% (Figure 2). This is especially critical for the UAV application as the operating temperature and pressure at the stack is expected to fall with altitude.

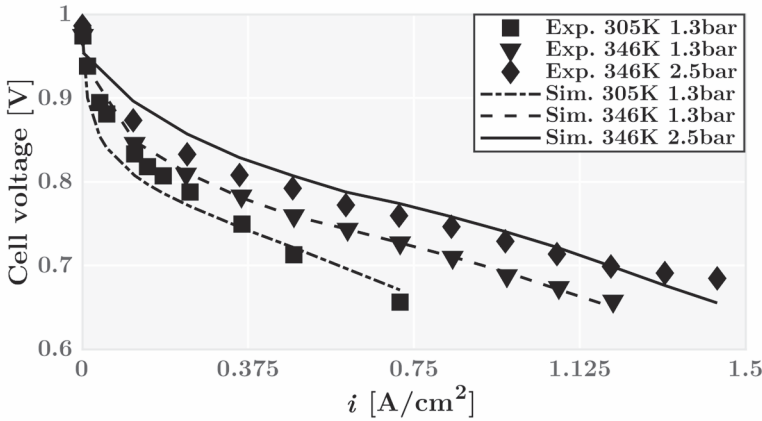


Figure 2. Fuel cell model validation with experimental data from [12,13] at different pressures and temperatures.

With the voltage, thus the power, calibrated for a wide range of current densities, the H_2 consumption is calculated as in Eq. 7:

$$\dot{m}_{H_2} = \frac{I n_{cell}}{2F} MW_{H_2} \tag{7}$$

where I is the stack current, n_{cell} is the stack number of cells, F is the Faraday constant and MW_{H_2} is the molecular mass of H_2 .

The number of cells in the stack was calculated in such a way that they produce 40 kW of power at the maximum current density. From preliminary calculations with the aerodynamic model, it was estimated that around 18 kW of net power would be required for cruise operation. As such, since around 20% of the maximum power of the stack is lost due to electrochemical losses and the BoP consumption at high load, 40 kW of maximum power was chosen to allow the FC stack to operate in the low-to-medium current density region where its efficiency is close to optimum and to have an additional margin when extra power is required [8]. The FC stack model was then integrated together with the models of the components of the BoP, thus conforming the FCS (figure 3).

The components of the BoP can be divided into those affecting the cathode circuit (air path), the anode circuit (H_2 path) and the coolant circuit. The cathode circuit consists of an electric compressor (e-compressor) in charge of providing pressurized air mass flow to the FC stack, a heat exchanger to cool down the air after the compressor, and a humidifier that uses the water at the outlet of the FC stack to increase the relative humidity at the cathode inlet to decrease the FC stack ohmic losses. For pressure and mass flow regulation purposes, the cathode circuit has a valve at its outlet that is controlled, as the power provided to the e-compressor, through a PID. The anode circuit consists of a H_2 tank, with a capacity to store 6 kg of H_2 , that provides the fuel feed to the stack through a pressure-regulating valve and an H_2 recirculating loop that controls the anode mass flow through the fuel pump. Finally, the cooling circuit controls the temperature at the outlet of the FC stack to 75°C by means of a radiator and

a refrigerant pump, as in most automotive applications. To know the detailed specifications of the BoP as well as the security limits and the anode and cathode stoichiometries the reader can refer to previous studies [8, 9].

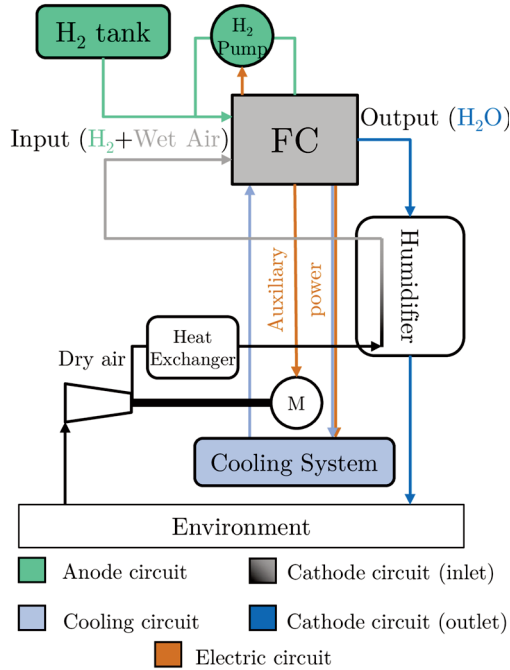


Figure 3. Fuel cell system outline integrating the FC stack and the components of the BoP [8].

The air management (e-compressor and cathode outlet valve control) was then optimized at different altitudes so that the operating cathode pressure and stoichiometry are optimum for any current density and altitude. This made the operation of the BoP close to optimum since the power consumption of the components used for the air management entails most of the BoP power consumption. The rest of the components (H₂ and coolant pumps) had almost negligible power consumption [8, 9]. Therefore, their operation was adjusted to ensure the safe operation of the stack by keeping its overall temperature close to 75°C and the anode stoichiometry around 3 to avoid starvation that could imply the FC accelerated degradation and performance decay. As in previous work, the optimized FCS model was simplified to a mean values model to decrease the simulation time, given the long time it takes for the UAV to carry out its mission (section 2.4).

The net power produced by the FCS then takes into account both the stack electrical power production and the BoP power consumption. A DC-DC converter with an efficiency of 95% was simulated at the output of the FCS to reproduce an indirect-type FCV architecture. This architecture is characterized by the presence of two different DC-DC converters for the FCS and the battery and a DC-AC converter for the e-motor (inverter). This architecture allows the downsizing of the FCS due to the voltage boost produced by the DC-DC converter and increases the lifetime of the stack since the DC-DC converter protects it against the electric fluctuations that may come from the DC bus [14].

2.2.2. E-motor and battery models

The conversion of the electrical energy produced by the FCS and the battery is carried out by a 60 kW electrical motor. Even though the FC stack maximum power is 40 kW the electric motor maximum power is always expected to be higher to have additional operation flexibility since the battery can provide extra power for take-off or in-flight performance. The maps used to model the electric motor were extracted from the experimental studies performed by Burress et al. [15] (Figure 4). Based on the mass and dimension data provided in this study the e-motor mass and inertia were estimated as 36.7 kg and $6.6 \cdot 10^{-3} \text{ kg m}^2$, respectively.

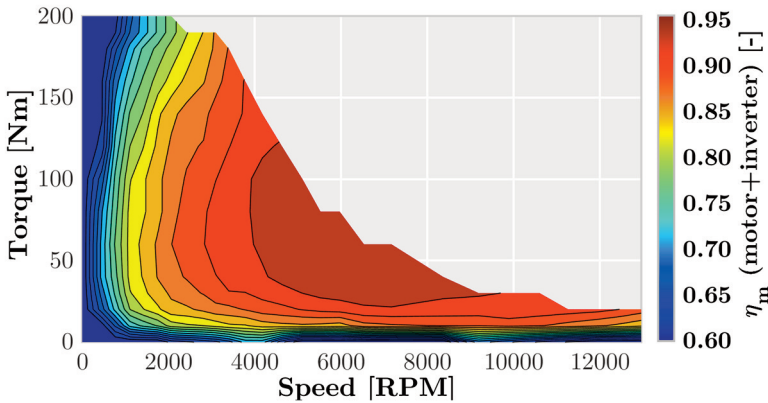


Figure 4. 60 kW e-motor map including motor mechanical efficiency and inverter electrical efficiency. Data extracted from [15].

The battery used to provide additional power to the electric motor when the power demand exceeds the maximum power production capability of the FCS is a Li-Ion battery consisting of 100 serial cells to ensure that the battery can provide high power when required grouped in 2 parallel circuits. The cells have a nominal voltage of 3.6 V and a nominal capacity of 3.35 Ah, hence a total battery pack capacity of 1.68 kWh taking into account that the battery can only be used between states of charge 0.2 and 0.9 to avoid accelerated degradation (70% of useful energy). The battery component was extracted from the GT-Suite platform and is based on a Thevenin electrical-equivalent battery model.

2.2.3. Propeller model

The selection of the propeller design is critical for the overall efficiency of the UAV as it sets the propulsive efficiency which represents the fraction of the mechanical energy produced by the e-motor that is converted into thrust power. As such, it must have high propulsive efficiency for the rotational speed at which the e-motor is expected to operate. The APC Propellers database was used to narrow down different propeller options to be used in the UAV model. Among the different possibilities explored, the propeller model was based on the performance curves of the propeller 16x5.5 MR. Although the diameter of this propeller design was scaled by a factor of 2, the blades were still operating at a Reynolds-independent speed and at a Mach number similar to that of the performance curves of the original propeller (see Figure 5).

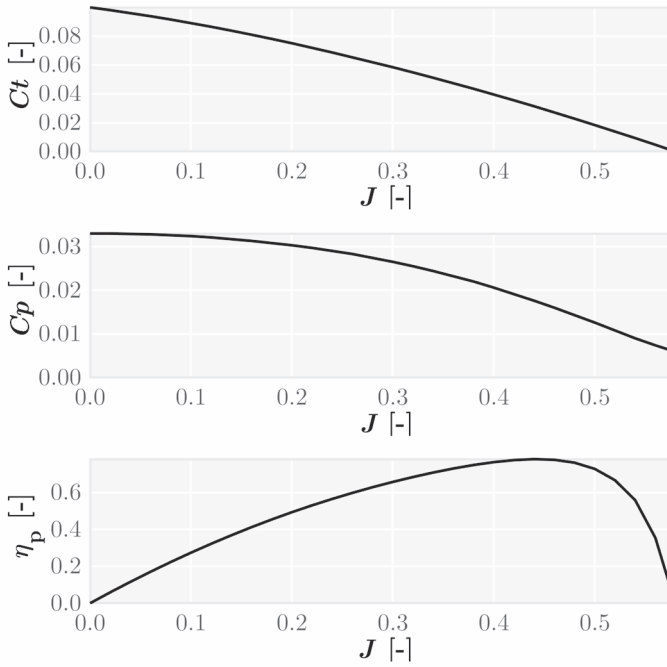


Figure 5. Propeller model: thrust coefficient (C_t), power coefficient (C_p) and propulsive efficiency (η_p) as a function of the advance ratio (J).

The usual equations for the advance ratio J , power coefficient C_p , thrust coefficient C_t and propulsive efficiency η_p are used, as presented in Eq. 8, 9, 10 and 11. In these equations, u is the airspeed, n is the rotational speed of the propeller, in Hz, D is the propeller diameter, P_{mb} is the propeller brake power, T is the propeller thrust and ρ is the air density.

$$J = \frac{u}{nD} \quad (8)$$

$$C_p = \frac{P_{mb}}{\rho n^3 D^5} \quad (9)$$

$$C_t = \frac{T}{\rho n^2 D^4} \quad (10)$$

$$\eta_p = \frac{C_t J}{C_p} \quad (11)$$

2.3. Aerial vehicle models integration

The models explained in sections 2.1 and 2.2 were integrated by connecting GT-Suite (FC, battery and e-motor models) with MATLAB (control strategy and UAV aerodynamic model). The flowchart in Figure 6 represents the model’s operation during simulation for a given time step dt . Every time-step a vector of discrete FCS power values (P_{FCS}) is evaluated as indicated in figure 6. The solution for each value of P_{FCS} is taken only when the advance ratio (J) and the propeller rotational speed (ω) converge with a relative error below 10^{-4} and 10^{-5} , respectively. The control of the FCS is performed through this iterative process as it aims to maximize the specific range calculated with the UAV aerodynamic model. The optimization problem was solved by applying the bisection method with adaptive discretization to minimize the error with low computational cost. Once the value of P_{FCS} that maximizes the specific range is found the model uses the selected value of u to compute the altitude for the next time step with the mission profile, and the converged value of ω to initialize the model in the next time step.

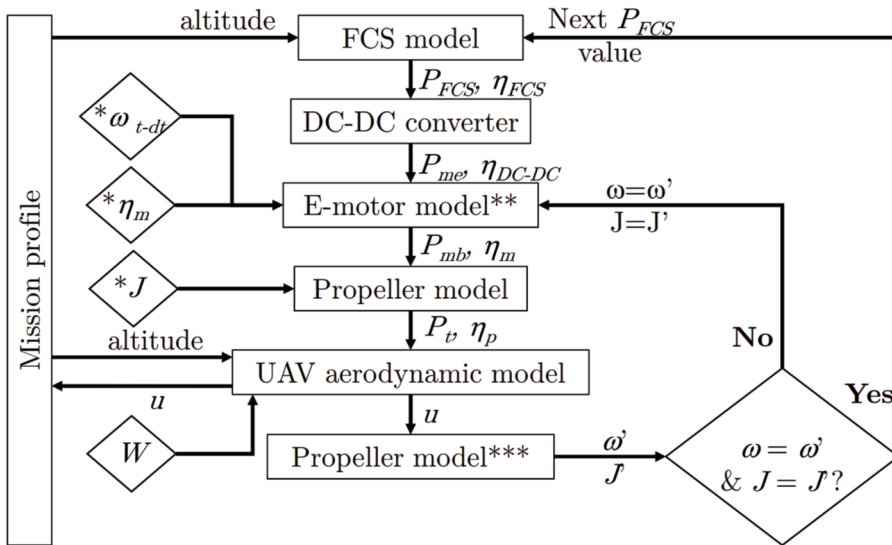


Figure 6. Model integration flow chart. P_{FCS} is the power provided by the FCS, η_{FCS} is the FCS efficiency, P_{me} is the e-motor electrical power demand, η_{DC-DC} is the DC-DC converter efficiency, P_{mb} is the e-motor brake power production, η_m is the e-motor and inverter efficiency, P_t is the thrust power produced, η_p is the propeller efficiency and W is the weight of the UAV.
 *Initialization values. ** η_m and P_{mb} are iterated until convergence for given values RPM and P_{me} .
 ***Used to iterate J and RPM for a given value of u .

Note that the weight of the UAV is updated continuously based on the H_2 consumption that corresponds the optimum P_{FCS} . For this application, even though the weight variation is small since there are only 6 kg of fuel stored, it was included in the model and had a small but noticeable effect on the mission performance.

The integrated models were then used to generate the performance maps of the UAV and for mission simulation (section 3). The former was done by calculating the performance parameters, such as systems efficiency, specific range and specific endurance, considering the MTOW at discrete values of P_{FCS} and altitude while the for the latter the mission profile was used to read the altitude as a function of the position, which was computed with the velocity and position in the previous time step, and the P_{FCS} was selected following the control strategy that maximizes the specific range.

2.3.1. Mass segmentation

Mass segmentation and estimation in aerial vehicles is critical to understanding the importance of the systems on the total weight of the aircraft and the room for payload they have to meet the requirements of a certain mission. As stated in section 2.1, the UAV aerodynamic model was based on the ATLANTE vehicle, with a MTOM of 570 kg [16]. To calculate the payload of the converted ATLANTE vehicle its operational empty weight (OEM) must be estimated. For that, the weight of the internal combustion engine (ICE) and the fuel of the original vehicle must be known. First, from the results in Figure 11, the maximum aerodynamic efficiency at a cruising altitude of 10,000 ft, which should be similar in the ATLANTE and the vehicle modeled, is roughly found at 15 kW of thrust power. From the propeller model, the propulsive efficiency at this point should be around 0.76–0.77 which results in an ICE nominal power of 20 kW. Knowing that the maximum power of the ICE for this application is usually twice the cruise power and that the specific power of compact engines is close to 1 kW/kg, the weight of the ICE was estimated as 40 kg. A reasonable value for the fuel consumption of a compact ICE in aerial applications is 0.4 kg/kWh, with a maximum endurance of 14 h [17] at cruising altitude and a fuel tank weight of 8 kg the total weight of the full fuel deposit should be 120 kg. If these weights, together with the maximum payload of 100 kg of the ATLANTE UAV [16], are subtracted from the MTOM, it results in an OEM of 310 kg. This value, albeit calculated roughly, could be considered a reasonable estimate of the OEM since all the hypotheses are in line with the usual values found for this application.

Table 1. UAV mass breakdown.

	Mass [kg]
MTOM	570
OEM	310
E-motor	36.7
FCS	49.2
H ₂ and tank	80
Battery	7.6
Power electronics	10
Payload	76.5

Once the OEM is calculated, the weight of the systems of the FCS-based powerplant should be added to obtain the maximum payload that the UAV can carry. For that, the electric motor weight was directly extracted from [15]. H₂ in the tanks for this application should be liquid to maximize specific range and endurance since the drone is expected to use most of the fuel for each mission, hence it can be loaded with fuel only before the mission and remain without while unused, thus avoiding the complete vaporization of liquid cryogenic H₂ in the tanks. Therefore, the gravimetric capacity of the tank should be 7.5 wt % [18] which implies a tank and fuel mass of 80 kg of which 6 kg are H₂. For the FCS weight, the specific power data provided by Department of Energy target for 2020 [19] was used (0.65 kW_{net}/kg). As commented in section 2.2.1, the FCS used in this study has a FC stack of 40 kW of maximum power at the limiting current density. This is translated to 32 kW of electrical net power to ensure stable operation after subtracting the consumption of the BoP components at a current density of 1.3 A/cm². Therefore, the FCS weight was estimated to be 49.2 kg. Finally, given the battery pack capacity of 1.68 kWh with an energy density of 0.22 kWh/kg [20] its weight should be 7.6 kg. This, added to an estimated weight of 10 kg for additional power electronics gives roughly a maximum payload capacity of 76.5 kg. A summary of these data can be found in Table 1.

Note that the payload decreased by 23.5% mainly due to the H₂ tank weight, which alone implies the 44% of the systems added to the drone.

2.4. Mission definition

A medium-altitude-medium-endurance (MAME) mission was selected to test the viability of the FC-powered UAV in a realistic scenario. This mission was designed to have the UAV operating at different altitudes for long distances. As such, the proposed mission describes the trajectory for a medical delivery from a hospital in Madrid to Mallorca Island (Figure 7), in Spain.

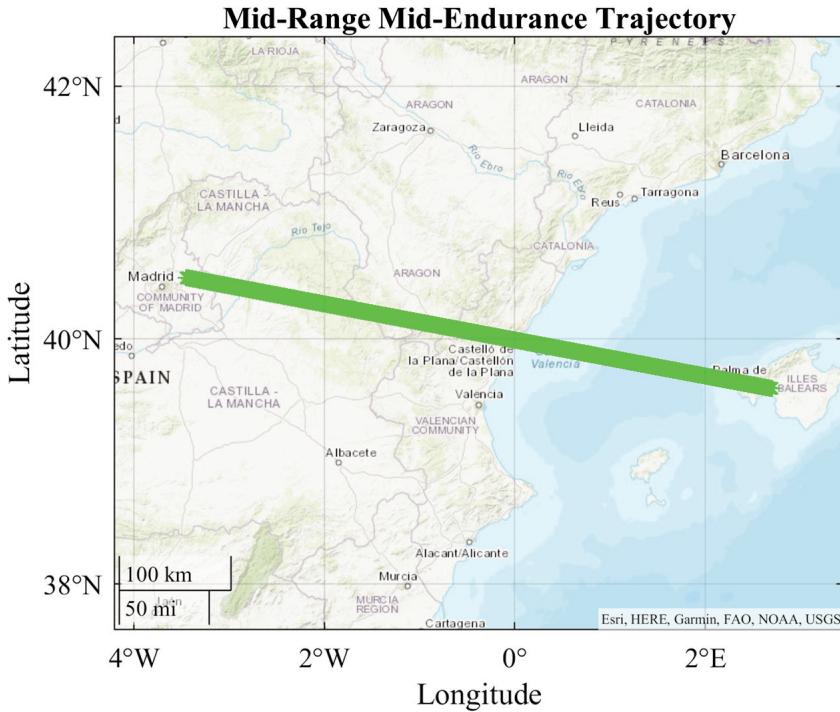


Figure 7. MAME mission trajectory.

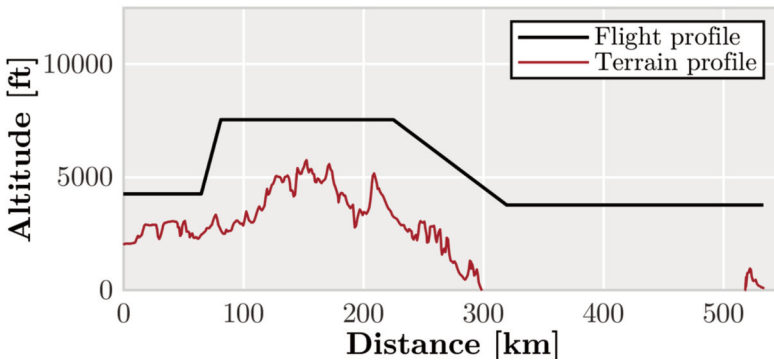


Figure 8. MAME flight and terrain profiles.

The mission range is 533 km and the flight profile was determined based on the terrain profile to avoid any collision. As a result, the vehicle flies at three different altitudes and has two transition phases (Figure 8): 1300 m (4265 ft), 2300 m (7546 ft) and 1150 m (3773 ft).

3. RESULTS AND DISCUSSION

The integrated model, as described in section 2.3, was then used to generate the maps in Figures 9–14. For that, the model was used to solve the UAV global and systems performance for different values of thrust power and altitude. This allows us to understand the change in performance of the different subsystems with the operating conditions and the decay in efficiency they may suffer from increased altitude. In the case of the FCS efficiency (Figure 9), the map was represented as a function of the FCS net power (thrust power divided by the propeller, e-motor and DC-DC converter efficiencies) to illustrate the effect of the load and the altitude on the system regardless of the application.

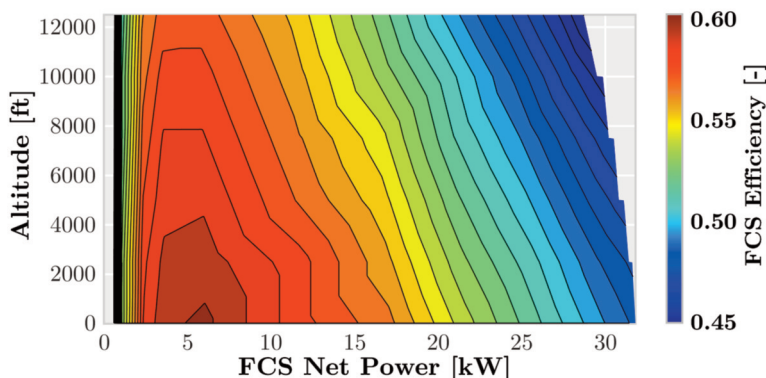


Figure 9. Contours of the FCS efficiency evolution with the altitude and the FCS net output power.

As explained in section 2.2.1, FCS efficiency includes the power consumption of the auxiliary components of the BoP and the FC stack electrochemical losses. As a consequence, its value oscillates between 0.4 and 0.6 in Figure 9. In these contours, the maximum FCS efficiency is found at low power (~ 5 kW, corresponding to the operating conditions on which the current density is low, hence the activation and ohmic losses are small, and the power consumption of the BoP components is also relatively low. Increasing or decreasing the load from this operating condition, regardless of the altitude, implies a decrease in the FCS efficiency. Increasing the load means an increase in both the electrochemical losses and the BoP consumption more significant than the increase in the FCS power output. In contrast, decreasing the load means decreasing the electrochemical losses and the BoP consumption. Nonetheless, the FC stack power is reduced in such a way that the BoP consumption is increased relative to the total power produced since it needs a minimum power input to keep the H_2 pump, coolant pump, and e-compressor working at the minimum load.

FCS net power can be converted to thrust power by multiplying it by the DC-DC converter, e-motor and propeller efficiencies. As such, for this application, taking into account that the minimum thrust power required for the UAV to maintain stable flight is 12 kW, the useful region in Figure 9 would be that with an FCS net power output higher than ~ 17.7 kW. This means that the FCS maximum efficiency for this application (achieved at 0 ft and minimum load) is 56% and could decrease to 45% if maximum load is required at higher altitude. The relatively high efficiency at worst-case condition is due to the flatness of the FC stack polarization curve, whose efficiency at constant altitude is always higher than 50% if the BoP management is optimized. Nonetheless, as seen in Figure 12, the optimum operation of the FCS to maximize range is within 13 to 16 kW of thrust power, i.e., 18–22 kW of FCS net output power. This means that for the selected mission, whose control was performed by adjusting the operation of all the systems to maximize range, the FCS efficiency should not be lower than 50%.

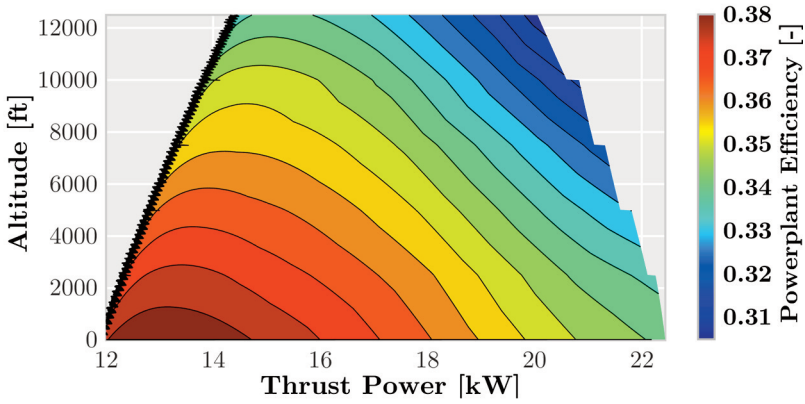


Figure 10. Contours of the powerplant efficiency evolution with the altitude and the thrust power.

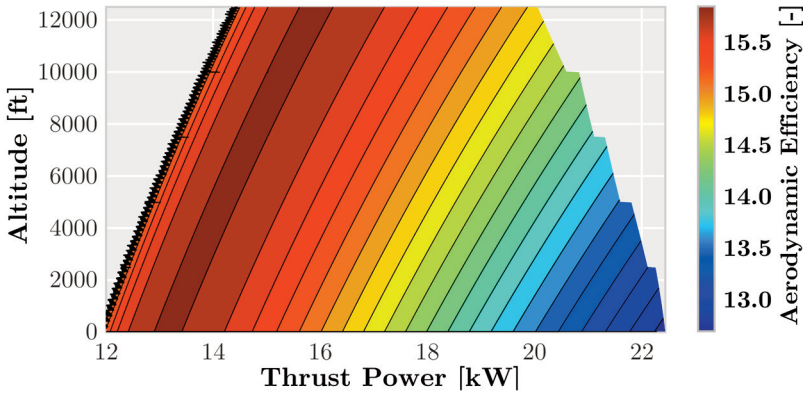


Figure 11. Contours of the UAV aerodynamic efficiency evolution with the altitude and the thrust power.

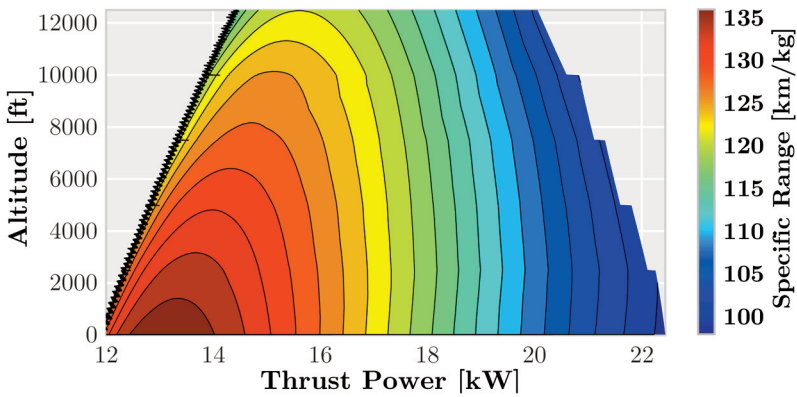


Figure 12. Contours of the UAV aerodynamic efficiency evolution with the altitude and the thrust power.

The FCS efficiency was then multiplied by the DC-DC converter, e-motor and propeller efficiencies, thus resulting in the total powerplant efficiency represented in the contours of Figure 10. Interestingly, the maximum powerplant efficiency does not correspond to the optimum operation of the FCS, thus implying that the flat behavior of the FCS efficiency makes the efficiency of the rest of the systems (mainly e-motor and propeller) become more relevant. This behavior allows the optimum operation of the powerplant to fall under that range of thrust power at which the UAV can fly with an optimum value ranging from 34% to 38% at each altitude.

The UAV optimum aerodynamic efficiency region falls close to the powerplant maximum efficiency at each altitude (Figures 10 and 11), thus maximizing the specific range at those operating conditions. This is a direct consequence of the selection of the propeller, which was chosen so it worked with maximum propulsive efficiency when flying at maximum aerodynamic efficiency, and by the flatness of the FCS efficiency. As expected, the maximum aerodynamic efficiency of the vehicle is almost independent of the flight altitude, and occurs at higher thrust powers and higher speeds when flying higher.

As inferred from the analysis of Figures 10 and 11, the maximum specific range of the selected vehicle is produced with a thrust power oscillating between 13 to 16 kW. In the contours of Figure 12, the specific range varies from 100 km/kg at maximum thrust power to 135 km/kg at optimum operating conditions at sea level. For low-altitude missions (3,200 ft), the optimum specific range is 133.8 km/kg with a thrust power of 13.8 kW, implying that a total cruise distance of 800 km could be covered with the 6 kg of H_2 the UAV can carry. At higher altitudes (10,000 ft), the maximum specific range decreases to 126.2 km/kg with a thrust power of 15.1 kW, i.e., a total cruise range over 750 km. Note that these ranges could be decreased if in-flight performances are usual and if take-off and landing are included. Nonetheless, similar range might be achieved with a correct sizing of the battery to support the UAV operation for a specific mission.

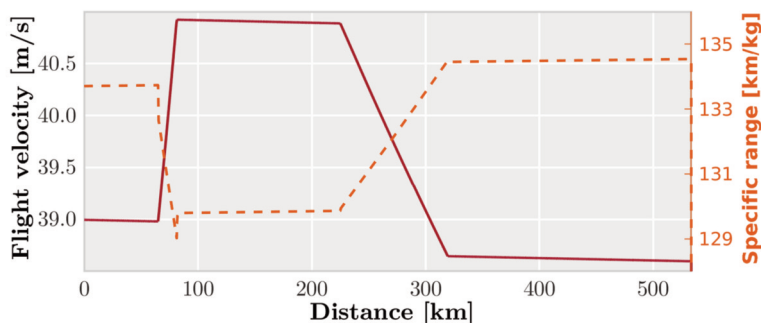


Figure 13. MAME flight speed and specific range during flight.

In the selected mission for this study, the flight altitude changes between 3,733 ft and 7,546 ft, meaning that the actual specific range for this mission could range from 128 to 135 km/kg, as shown in Figure 13, in which the flight speed is drawn as a solid, black line and the specific range is plotted with a dashed, red line. This means that performing the mission with the H_2 tank full is adequate for the required mission range (533 km) and provides an additional margin for take-off, landing, in-flight operation and even an eventual alternative airport landing. The tank capacity might be reduced in a real UAV design for this particular mission, thus increasing the payload capacity of the vehicle.

In terms of specific endurance, which is calculated by dividing the specific range by the flight velocity, the optimum operation is found at minimum thrust power for each altitude to minimize the H_2 consumption rate (Figure 14). The UAV operation that maximizes the flight duration allows specific

ranges oscillating between 52.8 min/kg at 10,000 ft and 62 min/kg at 3,200 ft. As a consequence, the maximum endurance with 6 kg of H₂ could be over 5 h, which may be adequate for surveillance missions close to aerodromes. The endurance of this vehicle falls by 65% compared to the original endurance of 14 h advertised by the manufacturer of the ATLANTE drone. Still, both its range and endurance are reasonable for aero-taxi and urban cargo transport applications but limited mainly by the weight of the H₂ tank (Table 1). Breakthroughs in the technology for H₂ storage, both liquid and gas, may significantly increase the range and endurance of FCS-powered aerial vehicles.

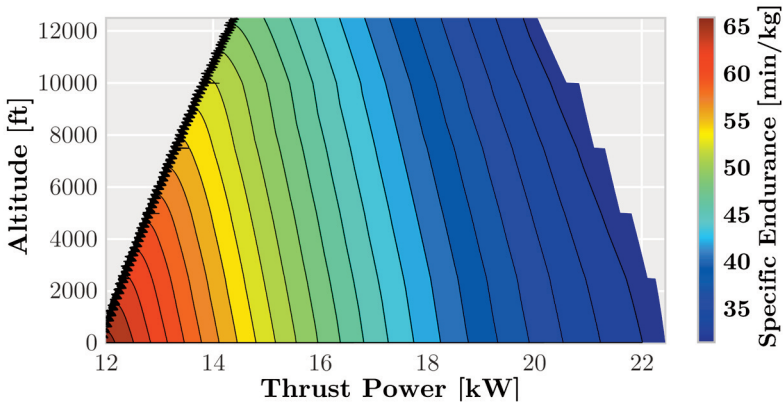


Figure 14. Contours of UAV specific endurance evolution with the altitude and the thrust power.

4. CONCLUSIONS

In this article, an analysis of a mission of a fixed-wing UAV with a payload capacity of 75 kg powered by a PEM fuel cell has been performed. For that, a tactical UAV, the ATLANTE aircraft by AIRBUS, has been used as a basis, computing its aerodynamic performance. A PEMFC has been sized for this application, as well as other parts of the system such as the propeller, the electric motor and the different DC-DC and DC-AC converters. With that, and using properly-calibrated models, a medium altitude, medium endurance mission has been simulated, showing promising results. Although the PEMFC-powered aircraft present non-negligible penalties in terms of endurance and payload capacity, it is nonetheless capable of performing useful missions with zero pollutant and CO₂ emissions. The PEMFC approach is expected to be a viable alternative to internal combustion engines to power aircraft in this segment, whose pure battery-electric propulsion systems do not seem to be able to achieve it without significant technological breakthroughs.

With a fuel cell stack with a maximum power roughly three times the minimum power required for cruise flight, the aircraft is able to operate with minimum expected stack degradation and very low ohmic losses, in the zone of maximum stack efficiency. This operating zone presents an efficiency that has been shown to be only weakly dependent on the flight altitude or speed, so the main efficiency changes in the whole systems are due to the BoP power consumption, the electric engine and the propeller. By carefully choosing all the components, the flight speed of maximum efficiency of all of them at different altitudes is more or less coincident, and similar to the minimum drag flight speed. This ensures a very high specific range and, thus, a small fuel consumption.

The total H₂ consumed during the mission studied here, a freight flight between two hospitals in Madrid and Mallorca, Spain, is well within what can be safely stored in a tank inside the aircraft. The fuel tank mass, however, is the main limiter of these applications: for a 1% of fuel mass when compared to

the MTOM, the total tank mass represents a 14%. Further developments in storage systems are expected to make the use of PEMFC in these missions much more attractive, leading to higher endurances, longer ranges and bigger payload capacities.

Acknowledgements: This research has been partially funded by the Spanish Ministry of Science, Innovation, and University through the University Faculty Training (FPU) program (FPU19/00550). This work is part of the project PID2020-119468RA-I00 funded by MCIN/AEI/ . Part of the research was also funded by Generalitat Valenciana and by “ERDF A way of making Europe” through grant number IDIFEDER/2021/039, as part of the program “Subvenciones para Infraestructuras y Equipamiento de I+D+i”. It was also partially funded by the Conselleria d’Innovació, Universitats, Ciència i Societat Digital of the Generalitat Valenciana through grant with expedient number GV/2021/069 of the program for “Grupos de Investigación Emergentes GV/2021”. The hydrogen activities were also funded by grant EQC2019-005968-P funded by MCIN/AEI/ and by “ERDF A way of making Europe”.

REFERENCES

- [1] European Commission, 2019, “A European Green Deal: Striving to be the first climate-neutral continent”, URL https://ec.europa.eu/info/strategy/priorities-2019-2024/european-green-deal_en.
- [2] European Commission, “European Partnership for Clean Aviation”, URL https://ec.europa.eu/info/law/better-regulation/have-your-say/initiatives/11904-European-Partnership-for-Clean-Aviation_en.
- [3] Chiaramonti, D. “Sustainable Aviation Fuels: the challenge of decarbonization.” *Energy Procedia* Vol. 158 (2019). pp. 1202–1207 DOI 10.1016/j.egypro.2019.01.308. Innovative Solutions for Energy Transitions.
- [4] Lee, S., Kim, G. and Bae, C. “Effect of injection and ignition timing on a hydrogen-lean stratified charge combustion engine.” *International Journal of Engine Research*. OnlineFirst (2021). DOI 10.1177/14680874211034682.
- [5] Caton, P.A. and Pruitt, J.T. “Homogeneous charge compression ignition of hydrogen in a single-cylinder diesel engine.” *International Journal of Engine Research* Vol. 10 No. 1. (2009). pp. 45–63. DOI 10.1243/14680874JER02208.
- [6] Christo, F.C., Levy, Y., Costa, M. and Balelang, G.A. “Effect of jet momentum flux and heat density on NOx emission in a flameless gas turbine combustor.” *Aerospace Science and Technology* Vol. 119 (2021). p. 107137. DOI 10.1016/j.ast.2021.107137.
- [7] Baroutaji, A., Wilberforce, T., Ramadan, M. and Olabi, A.G. “Comprehensive investigation on hydrogen and fuel cell technology in the aviation and aerospace sectors.” *Renewable and Sustainable Energy Reviews* Vol. 106 (2019). pp. 31–40. DOI 10.1016/j.rser.2019.02.022.
- [8] Molina, S., Novella, R., Pla, B. and Lopez-Juarez, M. “Optimization and sizing of a fuel cell range extender vehicle for passenger car applications in driving cycle conditions.” *Applied Energy* Vol. 285 (2021) p. 116469. DOI 10.1016/j.apenergy.2021.116469.
- [9] Desantes, J.M., Novella, R., Pla, B. and Lopez-Juarez, M. “Impact of fuel cell range extender powertrain design on greenhouse gases and NOx emissions in automotive applications.” *Applied Energy* Vol. 302 (2021). p. 117526. DOI 10.1016/j.apenergy.2021.117526.
- [10] Terada, I. and Nakagawa, H. “Polymer Electrolyte Fuel Cell.” *Kobunshi* Vol. 57 No. 7 (2008). pp. 498–501. DOI 10.1295/kobunshi.57.498.
- [11] Murschenhofer, D., Kuzdas, D., Braun, S. and Jakubek, S., “A real-time capable quasi-2D proton exchange membrane fuel cell model.” *Energy Conversion and Management*, Vol. 162 (2018). pp. 159-175. DOI 10.1016/j.enconman.2018.02.028.
- [12] Corbo, P., Migliardini, F. and Veneri, O. “Experimental analysis of a 20 kW PEM fuel cell system in dynamic conditions representative of automotive applications.” *Energy Conversion and Management* Vol. 49 No. 10 (2008). pp. 2688–2697. DOI 10.1016/j.enconman.2008.04.001.
- [13] Corbo, P., Migliardini, F. and Veneri, O. “Experimental analysis and management issues of a hydrogen fuel cell system for stationary and mobile application.” *Energy Conversion and Management* Vol. 48 No. 8 (2007). pp. 2365–2374. DOI 10.1016/j.enconman.2007.03.009.
- [14] Teng, T., Zhang, X., Dong, H. and Xue, Q. “A comprehensive review of energy management optimization strategies for fuel cell passenger vehicle.” *International Journal of Hydrogen Energy* Vol. 45 No. 39 (2020). pp. 20293–20303. DOI 10.1016/j.ijhydene.2019.12.202.

- [15] Burress, T.A., Campbell, S.L., Coomer, C.L., Ayers, C.W., Wereszczak, A.A., Cunningham, J.P., Marlino, L.D, Seiber, L.E. and Lin, H., "Evaluation of the 2010 Toyota Prius Hybrid Synergy Drive System.", Oak Ridge National Laboratory, Tennessee, USA. (2011).
- [16] Airbus Defence & Space. "Atlante: Tactical fixed wing multirole UAS for maximized operational capability and mission flexibility." (2014) URL <https://www.airbus.com/content/dam/products-and-solutions/unmanned-air-systems/atlante/atlante-brochure.pdf>.
- [17] Cassidian. "Atlante: Tactical Unmanned Aerial System for National Security." (2014) URL https://www.airtn.eu/downloads/atlante-para-airtn_v2.pdf.
- [18] Rivard, E., Trudeau, M. and Zaghbi, K. "Hydrogen storage for mobility: A review." *Materials* Vol. 12 No. 12 (2019). DOI 10.3390/ma12121973.
- [19] U.S. Department Of Energy. "DOE Technical Targets for Fuel Cell Systems and Stacks for Transportation Applications." (2015). URL <https://www.energy.gov/eere/fuelcells/doe-technical-targets-fuel-cell-systems-and-stacks-transportation-applications>.
- [20] Howell, D., Cunningham, B., Duong, T. and Faguy, P. "Overview of the DOE VTO Advanced Battery R&D Program." U.S. Department Of Energy (2016).